

SURFACE TEMPERATURE OF A MAGNETIZED NEUTRON STAR AND INTERPRETATION OF THE *ROSAT* DATA. I. DIPOLAR FIELDS

Dany Page

Instituto de Astronomía, UNAM, Apdo Postal 70-264, 04510 México D.F., México ¹
Department of Astronomy, Columbia University, New York, NY 10027, USA

ABSTRACT

We model the temperature distribution at the surface of a magnetized neutron star and study the effects on the observed X-ray spectra and light curves. General relativistic effects, i.e., red-shift and lensing, are fully taken into account. Atmospheric effects on the emitted spectral flux are not included: we only consider blackbody emission at the local effective temperature. In this first paper we restrict ourselves to dipolar fields. General features are studied and compared with the *ROSAT* data from the pulsars 0833-45 (Vela), 0656+14, 0630+178 (Geminga), and 1055-52, the four cases for which there is strong evidence that thermal radiation from the stellar surface is detected.

The composite spectra we obtain are not very different from a blackbody spectrum at the star's effective temperature. We conclude that, as far as blackbody spectra are considered, temperature estimates using single temperature models give results practically identical to our composite models. The change of the (composite blackbody) spectrum with the star's rotational phase is also not very large and may be unobservable in most cases.

Gravitational lensing strongly suppresses the light curve pulsations. If a dipolar field is assumed, pulsed fractions comparable to the observed ones can only be obtained with stellar radii larger than what predicted by current models of neutron star structure, or with low stellar masses. Moreover, the shapes of the theoretical light curves with dipolar fields do not correspond to the observations. The use of magnetic spectra may rise the pulsed fraction sufficiently, but will certainly make the discrepancy with the light curve shapes worse: dipolar fields are not sufficient to interpret the data. Many neutron star models with a meson condensate or hyperons predict very small radii, and hence very strong lensing, which will require highly non dipolar fields to be able to reproduce the observed

¹Current address.

pulsed fractions, if possible at all: this may be a new tool to constrain the size of neutron stars.

The pulsed fractions obtained in all our models increase with photon energy: the strong decrease observed in Geminga at energies 0.3 - 0.5 keV is definitely a genuine effect of the magnetic field on the spectrum in contradistinction to the magnetic effects on the surface temperature considered here. Thus, a detailed analysis of thermal emission from the four pulsars we consider will require both complex surface field configurations and the inclusion of magnetic effects in the atmosphere (i.e., on the emitted spectrum).

Subject headings: dense matter — stars: neutron — stars: X-rays

Submitted to *The Astrophysical Journal*

1. INTRODUCTION

The detection of thermal emission from the surface of a neutron star is one of the ‘Holy Graal’s of X-ray astronomy. At the first detection of X-rays from the direction of the Crab supernova remnant, surface thermal radiation from the neutron star already expected to be present in this remnant was proposed as the most probable source (Bowyer *et al.* 1964), but the claim was soon disproved and even the most recent *ROSAT* observation of the Crab pulsar failed to detect any emission from the surface (Becker & Aschenbach 1993). A compilation of all *Einstein* observations (Seward & Wang 1988) listed ten neutron stars detected in soft X-rays, to which should now be added Geminga which at that time was not yet proved to be a neutron star but had been clearly seen by *Einstein* (Bignami, Caraveo & Lamb 1983). As of August 1993 there were thirteen confirmed detections of pulsars by *ROSAT* and six unconfirmed ones (Ögelman 1993). In most cases the radiation is probably of magnetospheric origin with some contamination from the surrounding synchrotron nebula, at least for the younger candidates, and surface thermal emission in some cases. With the sensitivity of the *ROSAT*’s PSPC (Position Sensitive Proportional Counter) and long exposure times there is now strong spectral evidence that thermal radiation has been detected from four neutron stars (Ögelman 1993): PSR 0833-45 (Vela) (Ögelman, Finley & Zimmermann 1993), PSR 0656+14 (Finley, Ögelman & Kiziloğlu 1992), PSR 0630+178 (Geminga) (Halpern & Holt 1992), and PSR 1055-52 (Ögelman & Finley 1993). Moreover, these four objects show pulsed X-ray emission, three of them (except Geminga) are radio pulsars and three (except PSR 0656+14) have also been detected as γ -ray pulsars.

Earlier *Einstein* observations had already provided some limited evidence for detection of surface thermal radiation in the cases of the Vela pulsar (Harnden *et al.* 1985), PSR 0656+14 (Córdova *et al.* 1989), and Geminga (Halpern & Tytler 1988), while in the case of PSR 1055-52 (Cheng & Helfand 1983) thermal emission was considered as incompatible with the data. In later *EXOSAT* observations, with broad band spectroscopy only, thermal radiation was considered as the most reasonable origin of the detected soft X-rays in both cases of the Vela pulsar (Ögelman & Zimmermann 1989) and PSR 1055-52 (Brinkmann & Ögelman 1987). Because of its late discovery, as an X-ray source, in the *Einstein* data base, PSR 0656+14 has not been observed by *EXOSAT*. The *EXOSAT* observation of Geminga (Caraveo *et al.* 1984) did not give any new spectral information compared to the *Einstein* results. A review of the pre-*ROSAT* observational situation has been given by Ögelman (1991).

The quality of the *ROSAT* data from these four nearby neutron stars presents a new challenge for theorists to provide good models for their interpretation. The heretofore published analyses of these data have all assumed a unique surface temperature, with at

most a second thermal component coming from the small hot polar caps. We model here the temperature distribution at the surface of a magnetized neutron star and study its effects on the received spectra and light curves. The crustal magnetic field affects the heat transport in the layers beneath the surface and makes that regions of the star where the field is almost normal to the surface will be warmer than regions where the field is almost tangential to the surface. These temperature differences will give rise to modulation of the received flux at energies between 0.1 and 1 keV and are a natural explanation for the observed pulsations in the above mentioned four neutron stars. This long searched for detection of thermal radiation from the surface of neutron stars thus opens up a new window in the study of these objects. It has the potential to tell us about the structure of the surface magnetic field and give us new information about the size of these stars through gravitational lensing effects which obviously will be substantial. Our purpose in this first paper is to present the general physics involved and study the simplest case of a dipolar surface magnetic field. We have tried to present as clearly as possible the underlying physical ingredients as well as the method used, laying hopefully a clear groundstone for future improvements and/or modifications.

General relativistic effects may be enormous in neutron stars and we take fully into account both gravitational red-shift and gravitational lensing. Magnetic fields are also affected by strong gravitational fields but we do not consider this effect: of critical importance for the surface temperature distribution is the angle between the surface's normal and the magnetic field, and this angle is practically unaffected by gravity (Ginzburg & Ozernoy 1964). The major effect of gravity on the surface magnetic field is to increase its strength at small radii: for a given dipolar field at infinity the surface strength is increased by 20-50% by gravity compared to the value it would have in flat space-time. The surface field strengths we consider should thus simply be somewhat reduced for comparison with values obtained for example from pulsar spin-down. Our results are however not very sensitive to changes of this size in the field strength. We do not include the effects of the magnetic field on the atmosphere where the emitted spectrum is determined. These effects are also substantial and will hopefully be included in future work.

It has been proposed that the surface of neutron stars may be a magnetic solid (Ruderman 1974; Chen, Ruderman & Sutherland 1974). Even if improved calculations of the atomic lattice cohesive energy in very strong magnetic fields have indicated that this is not the case (Jones 1986), one should nevertheless keep in mind this possibility. It would obviously have dramatic effects on the emitted spectrum (Brinkmann 1980) and some, comparatively smaller, effect on the surface temperature (see Van Riper 1988 for simple estimates) Our model is based on magnetized envelope calculations which assume that the surface is not a magnetic solid: would this be uncorrect, our results should clearly be

reconsidered.

We must also mention that the interpretation presented here assumes that the surface temperature is determined by the flow of heat from the star’s interior and thus carries the imprint of the underlying crustal magnetic field. Another interpretation has been proposed (Halpern & Ruderman 1993) in which the hard X-rays emitted by the hot polar caps are scattered back onto the surface by the magnetospheric plasma: if this is the case the surface temperature has nothing to do with the properties of the magnetized envelope and our model is then obviously irrelevant. A composite model is also possible: the general temperature distribution may be determined by the heat flow from the interior and some regions heated by the back scattered hard X-rays. Moreover, absorption and scattering of radiation by the surrounding magnetospheric plasma may also be an important factor in reshaping the emitted flux (Halpern & Ruderman 1993). Which of these possibilities is actual can only be determined by studying each of them carefully. This paper is a first step in that direction.

The structure of the paper is as follows. The *ROSAT* data are summarized in § 2. where we emphasize the features relevant to our purpose. In § 3. we describe the effects of the magnetic field on heat transport in the envelope and our model for the surface temperature distribution and in § 4. we present the method used to calculate the fluxes as observed by *ROSAT*. Our results are in § 5. and they are discussed in § 6., followed by our conclusions in § 7.

2. THE *ROSAT* DATA

We present in this section some characteristics of the *ROSAT* data for the four neutron stars we study along with some relevant informations obtained at other energies, summarized in Table 1. Vela is the younger of the four and an accurate estimate of its surface temperature is of outmost importance since it could give us evidence for the occurrence of fast neutrino emission in its early cooling history (Page & Applegate 1992). The other three are much older and their importance for cooling is distinct; they do provide us with insight about the state of their interior (Page 1994a). All four are X-ray pulsars, three of them (except Geminga) are also radio pulsars, three (except PSR 0656+14; see however Ma *et al.* 1993 and Brown & Hartmann 1993) are γ -ray pulsars and three (except PSR 1055-52) have an optical counterpart. Analysis of the X-ray emission from the Vela pulsar is delicate because of the strong emission from the surrounding synchrotron nebula which has to be subtracted from the data to obtain the signal from the pulsar itself. The

other three X-ray sources are much cleaner than Vela: there is no evidence of extended emission in the *ROSAT* HRI observation of PSR 0656+14 (Anderson *et al.* 1993) and PSR 1055-52 (Ögelman & Finley 1993). There is no HRI observation of Geminga to date but the PSPC data are compatible with a point source.

All four objects show pulsed X-ray emission within the *ROSAT* energy range (0.08 - 2.5 keV) and a two component spectrum, the soft component (roughly below 0.5 keV) being interpreted as surface thermal emission (Ögelman 1993). The corresponding pulsed fractions of these soft components are listed in Table 1. Geminga’s pulsed fraction below 0.28 keV is larger than between 0.28 - 0.5 keV while the other three pulsars have a roughly constant pulsed fraction below 0.5 keV (a slight decrease seems to be present in PSR 1055-52 below 0.5 keV). The phase of the peak in the light curve of these soft components is independent of the photon energy; the peaks are broad, the flux being above its mean value more than 50% of the time; the light curves are non sinusoidal. The hard component of Vela appears to be unpulsed: it may be real or just due to the fact that count rates are low in this part of the spectrum and the signal has been extracted from the nebula emission. In the case of PSR 0656+14 the count rate is too low to detect pulsation of the hard component but in the other two cases (Geminga and PSR 1055-52) pulsations are clearly seen and they are substantially off-phase compared to the soft component. The origin of the hard component of these spectra still remains elusive due to the low count rates, fits with blackbody or power-law spectra giving equally good (or bad) results. It could be thermal emission from the hot polar caps or some magnetospheric process coming maybe, but not necessarily, from just above the polar caps. In this paper ‘soft’ and ‘hard’ X-rays will always refer to these two components within the *ROSAT* energy range.

The effective temperatures T_e^{BB} and interstellar column densities N_H^{BB} listed in Table 1 were obtained from single temperature blackbody fits. In the case of Vela, the quoted effective temperature and the observed flux imply a stellar radius of 3-4 km, i.e., only 10% of the surface is emitting at this temperature: this may be due to very large surface temperature gradients or to a strong inadequacy of the blackbody spectrum. Use of more complex spectra from non magnetized He atmosphere (Romani 1987) or magnetized H atmosphere (Pavlov *et al.* 1994) give lower temperatures: $2.2 - 2.6 \times 10^5$ K (Finley *et al.* 1992) and $6.6 - 7.4 \times 10^5$ K (Anderson *et al.* 1993) respectively instead of $8.6 - 9.4 \times 10^5$ K with a blackbody spectrum in the case of PSR 0656+14. In the case of Geminga, magnetized hydrogen atmosphere spectra also give lower temperatures, $2 - 3 \times 10^5$ K (Meyer *et al.* 1994).

The (dipolar) magnetic field strengths we cite are obtained the standard way (magnetic

dipole radiation braking) by

$$B_p = 2 \times 10^{12} (P \dot{P}_{-15})^{1/2} \text{G} \quad (1)$$

where P is the period in seconds and \dot{P}_{-15} its derivative in units of $10^{-15} \text{ s s}^{-1}$. B_p is thus the field strength at the magnetic pole on the star’s surface. These values are of course only indicative, and general relativistic strengthening of the surface field adds to this uncertainty. Phenomenological analyses of the radio data allow to estimate the inclination angle α of the dipole with respect to the rotation axis and the angle ζ between the observer’s direction and the rotation axis, but the results are strongly model dependent in many cases (Miller & Hamilton 1993). PSR 1055-52 is generally considered as a typical example of radio inter-pulsar where emission from both magnetic poles is detected ($\alpha \sim \zeta \sim 90^\circ$); an alternative explanation for the interpulse is that the same magnetic pole is seen twice per rotation ($\alpha \sim \zeta \sim 0^\circ$). In the case of Geminga, modeling of the γ -ray emission within both the outer gap (Halpern & Ruderman 1993) and polar cap (Harding, Ozernoy & Usov 1993) models indicate that $\alpha \sim \zeta \sim 90^\circ$. The beaming of radio emission obviously requires $\alpha \sim \zeta$ for radio pulsars.

3. STRUCTURE OF THE ENVELOPE

For all neutron stars we are presently interested in, the interior is isothermal and a temperature gradient only appears in the upper layers of the outer crust (Nomoto & Tsuruta 1986, 1987). We will call these layers the *envelope* and fix its upper density at $\rho = 10^{10} \text{ gm/cm}^3$. On top of the envelope resides the *atmosphere*: the total energy flux reaching it is determined within the underlying envelope, mostly by electron transport, and cannot be changed anymore, but its energy distribution, i.e., the emitted spectrum, is determined here.

3.1. Envelope without magnetic field

Detailed calculations of heat transport in non magnetized neutron star envelopes have been presented by Gudmundsson, Pethick & Epstein (1982, 1983) and Hernquist & Applegate (1984) These authors noticed that the study of the envelope can be separated from the study of the interior, since for neutron stars several months old the evolution time

scale of the interior is much larger than the thermal time scale of the envelope, and the latter can be considered to be in a steady state. The structure of the envelope depends on the gravitational acceleration at the surface

$$g_s = \frac{GM}{R^2 \sqrt{1 - 2GM/Rc^2}} \quad (2)$$

and on the temperature at its base T_b , i.e., at the envelope-interior boundary at density $\rho = 10^{10} \text{ gm cm}^{-3}$. Since the interior is isothermal its temperature is $T_{int} = T_b$. The envelope then determines the effective temperature T_e related to the interior temperature T_b quite accurately by

$$T_{b8} \cong 1.3 \left(\frac{T_{e6}^4}{g_{s14}} \right)^{0.455} \quad (3)$$

(Gudmundsson, Pethick & Epstein 1982) where X_n is X measured in 10^n cgs units. Since the interior is isothermal and, in absence of magnetic field, the heat transport in the envelope is isotropic the resulting surface temperature is uniform over the star: $T_s(\theta, \phi) = T_e$.

The heat transport is due to electrons in the lower layers and to photons in the upper layers. The critical region, “sensitivity strip”, which determines the $T_b - T_e$ relationship is the region just below the electron-photon transport transition where heat is thus transported mainly by electrons and the ions are in the liquid phase (Gudmundsson, Pethick & Epstein 1982, 1983; Hernquist & Applegate 1984). When the surface temperature decreases below about $\sim 3 \cdot 10^5$ K, the sensitivity strip is mostly in a region where the ions are partially ionized and there is no reliable calculation of the electron conductivity in this regime. Electron scattering by impurities also begins to contribute significantly; it depends on the impurity concentration, at most a poorly known quantity. Moreover the photon opacity has to be extrapolated significantly from calculated values. This makes that the surface temperatures cannot be reliably calculated and all such values ($T_s < 3 \cdot 10^5$ K) are only illustrative. The same remark apply *a fortiori* to the magnetic cases considered in the next subsection.

3.2. Envelope with magnetic field

In presence of a strong magnetic field the electron motion in directions perpendicular to the field becomes quantized, the electrons occupying Landau levels with spacings (non

relativistic case)

$$\hbar\omega_B = \frac{\hbar|e|B}{m_e c} = 11.3 \text{ keV } B_{12} \quad (4)$$

For typical fields present in neutron star envelopes electrons will occupy, at zero temperature, only the first Landau level up to densities of the order of $5 \cdot 10^5 \text{ gm cm}^{-3}$ and then start to populate higher levels. Temperature can push electrons into higher levels only when

$$k_B T \gg \hbar\omega_B. \quad (5)$$

The structure of the electron Fermi surface is thus strongly affected by the magnetic field almost across the whole sensitivity strip, and the transport properties will consequently depend on the field. Electron transport in directions perpendicular to the field is strongly suppressed while it is slightly enhanced parallelly to the field. Photon opacities are also affected but the Rosseland mean, the relevant quantity for heat transport, is only slightly anisotropic: anisotropy in heat transport thus comes mainly from electrons. A review of magnetized envelopes can be found in Yakovlev & Kaminker (1994).

When compared to the non magnetic case, the surface temperature will be slightly higher if the magnetic field is radial (parallel transport) but much lower if the magnetic field is tangential to the surface (orthogonal transport). The envelope being at most a few tens of meters thick one can safely assume that the magnetic field is uniform across it. Detailed modelling of magnetized neutron star envelopes with uniform field have been presented by Hernquist (1985), Van Riper (1988) and Schaaf (1990a) for the case of parallel transport while the only published models for orthogonal transport are given by Schaaf (1990a). Hernquist’s (1985) and Van Riper’s (1988) results are in good agreement except at low temperature where Van Riper’s inclusion of the (negative) ion Coulomb pressure (omitted by Hernquist) showed that the magnetic effects on the equation of state become dominant (Schaaf’s results are not in such good agreement due probably to the many approximations done). For the relevant field strengths, these magnetic $T_b - T_s$ calculations can hence only be trusted at $T_s \gtrsim 3 \cdot 10^5$ K, the same range of validity as for the non magnetic case. We will use Hernquist’s (1985) results for parallel transport and Schaaf’s (1990a) results for orthogonal transport. Figure 1 shows the resulting $T_b - T_s$ relationships.

In the particular cases of transport with a radial or a tangential field the problem is one dimensional since the heat flux can only be radial by symmetry. For an arbitrary orientation of the field with respect to the radial direction the problem of heat transport becomes two-dimensional. However, if the field orientation is sufficiently uniform on a length scale of a few tens of meters (= thickness of the envelope) the problem can locally be reduced to one dimension, at least in a first approximation. The surface temperature T_s then depends only on the field strength B and the angle Θ_B between the field and the

radial direction (beside the dependence on the envelope’s bottom temperature T_b and the surface gravitational acceleration g_s). Greenstein & Hartke (1983) showed that one can then approximately write (keeping only the Θ_B dependence explicit)

$$T_s(\Theta_B) = \chi(\Theta_B) \times T_s(\Theta_B = 0) \quad (6)$$

where

$$\chi(\Theta_B) = [\cos^2 \Theta_B + \chi_0^4 \sin^2 \Theta_B]^{1/4}. \quad (7)$$

In Greenstein & Hartke’s argument $\chi_0^4 = K_\perp/K_\parallel$, the ratio of the thermal conductivities perpendicular and parallel to the magnetic field, which is assumed to be constant within the envelope. The Figure 1 gives the values of T_s at $\Theta = 0^\circ$ and 90° and we will use Equ. 6 and 7 to define T_s at intermediate angles, thus taking

$$\chi_0 \equiv \frac{T_s(\Theta = \pi/2)}{T_s(\Theta = 0)}. \quad (8)$$

Two main approximations are done in deriving Equ. 6 and 7. The first one is that the radial temperature gradient dT/dr is much larger than the meridional temperature gradient dT/dx (x being a coordinate along the star’s surface): T drops by about two orders of magnitude across the envelope whose thickness is only a few tens of meters, while it varies by less than a factor 10 (see Fig. 1) along the surface on length scales of kilometers, thus $dT/dr \gg dT/dx$. The second approximation is that the thermal conductivities K_\parallel and K_\perp are constant: Hernquist & Applegate (1984) showed that in fact, in the non magnetic case, the temperature profile $T(\rho)$ within the outer part of the envelope where the conductivity is dominated by the photons (the region where most of the temperature drop occurs) does follow a trajectory of constant K . The validity of Equ. 6 and 7 can however only be checked by comparison with two-dimensional calculations. Schaaf (1990b) has performed such a calculation with relative success and many approximations which make it far from definitive, but his results are well reproduced by these simple formulas Equ. 6 and 7. Awaiting a more detailed study, Equ. 6 and 7 are the best that can be done.

3.3. The atmosphere and the emerging spectrum

The structure of the atmosphere is of critical importance for observations. The total flux permeating it is controlled by the underlying envelope but the spectral distribution of the flux (i.e., the emerging spectrum) is determined in this region. In the present work we will assume for simplicity that this emerging spectrum is a blackbody spectrum. Romani

(1987) took into account various possible chemical compositions of the atmosphere to calculate more realistic spectra in a zero magnetic field approximation. Due to the general ω^{-3} frequency dependence of the opacity $\kappa(\omega)$ of a non magnetic fully ionized plasma, the specific flux is increased at high frequencies, reduced at low frequencies, and differs substantially from a blackbody spectrum. When partial ionization is taken into account the excess in the Wien part of the spectrum is reduced, the effect being most dramatic when metals are present. For most relevant temperatures, this part of the spectrum lies within the *Einstein* and *ROSAT* detector ranges. Inclusion of the magnetic effects is an enormous challenge and extensive calculations are in progress (Shibanov *et al.* 1992; Pavlov *et al.* 1994). For a fully ionized magnetic plasma $\kappa^B(\omega) \sim \omega^{-1}$ and the resulting spectrum is intermediate between the blackbody and the fully ionized non magnetic spectrum. Since the magnetic field increases substantially the electron binding energies, hydrogen absorption edges are present even at high temperature and alter the spectrum precisely within the detector ranges, pushing it toward the Planck spectrum or even below at low enough temperature (the details of these absorption edges are unfortunately blurred by the PSPC’s low energy resolution).

The blackbody approximation may finally not be as bad as it appeared originally in Romani’s work. Moreover, the magnetic spectra depend on many parameters which have to be added to the parameter set of the models presented here and will make the analysis much more complicated. For these reasons, in this first work, we will consider only blackbody emission, characterized by the local effective temperature, and reserve more realistic spectra for future work.

4. GENERATING LIGHT CURVES AND SPECTRA

4.1. Flat Space-time

Assume we have a neutron star at a distance D from the observer and we want to calculate the number of photons of energy E reaching a detector whose effective area for these photons is $A(E)$. Choosing spherical coordinate (θ, ϕ) on the star’s surface with the coordinate axis pointing toward the detector, the number of photons emitted at the surface by an area $d^2A = R^2 \sin \theta d\theta d\phi$, where R is the star’s radius, is

$$d^6N = \text{Phase Space Volume} \times \text{Distribution Function} = 2 \frac{d^3x d^3p}{h^3} \times n(E, T; \dots) \quad (9)$$

where the distribution function n may depend, beside the photon energy E and the temperature T of the emitting region d^2A , on the local magnetic field, chemical composition, etc... For blackbody emission $n = 1/(e^{E/k_B T} - 1)$. Let's write

$$d^3x = c dt \cdot d^2A \cos \theta \quad (10)$$

(c is the speed of light and dt the time during which the received photons have been emitted) and

$$d^3p = p^2 dp d\Omega_p = \frac{E^2 dE}{c^3} \frac{A(E)}{D^2} \quad (11)$$

($d\Omega_p = A(E)/D^2$ is the detector's solid angle as seen from the star's surface and $p = E/c$ the photon momentum), and integrate the emission over the portion of the star visible to the observer. Interstellar absorption at energy E is included through a factor $\exp(-N_H \sigma(E))$, where N_H is the effective hydrogen column density between the star and the observer and $\sigma(E)$ the effective cross section (Morrison & McCammon 1983). We obtain thus

$$d^2N(E) = \frac{2\pi}{c^2 h^3} \frac{R^2}{D^2} \langle n(E; \dots) \rangle e^{-N_H \sigma(E)} E^2 A(E) dt dE \quad (12)$$

where

$$\langle n(E; \dots) \rangle \equiv \int_0^1 2x dx \int_0^{2\pi} \frac{d\phi}{2\pi} n(E, T(\theta, \phi); \dots) \quad (13)$$

is the distribution function averaged over the visible part of the star and $x \equiv \sin \theta$.

4.2. Curved Space-time

General relativistic effects are twofold here: red-shift and lensing. The red-shift makes that photons emitted at energy E are received at energy $E_\infty = Ee^\phi < E$ while photons emitted during a time dt are received in a time $dt_\infty = e^{-\phi} dt > dt$ where

$$e^\phi \equiv \sqrt{1 - \frac{2GM}{Rc^2}} < 1. \quad (14)$$

With this we can rewrite the photon flux in term of observed quantities as

$$\begin{aligned} d^2N(E_\infty) &= \frac{2\pi}{c^2 h^3} \frac{R_\infty^2}{D^2} \langle n(e^{-\phi} E_\infty; \dots) \rangle e^{-N_H \sigma(E_\infty)} E_\infty^2 A(E_\infty) dt_\infty dE_\infty \\ &\equiv \mathcal{N}(E_\infty) A(E_\infty) dt_\infty dE_\infty \end{aligned} \quad (15)$$

where

$$R_\infty \equiv R e^{-\phi} = \frac{R}{\sqrt{1 - \frac{2GM}{Rc^2}}} > R \quad (16)$$

and the photon flux $\mathcal{N}(E_\infty)$ has dimension [photons $\text{cm}^{-2} \text{sec}^{-1} \text{keV}^{-1}$].

The effect of gravitational lensing on photons emitted by hot spots on the surface of neutron stars has been studied in detail by Pechenick, Ftaclas & Cohen (1983). More than half of the star’s surface is visible to an observer at infinity (Fig. 2) and a photon emitted at collatitude θ on the star’s surface which reaches the observer must be emitted at an angle δ to the star’s normal, defined through

$$\theta = \theta(x) = \int_0^{GM/Rc^2} \frac{x \, du}{\sqrt{\left(1 - \frac{2GM}{Rc^2}\right) \left(\frac{GM}{Rc^2}\right)^2 - (1 - 2u)u^2 x^2}}. \quad (17)$$

where

$$x \equiv \sin \delta. \quad (18)$$

The impact parameter b of the photon trajectory is then given by $b = x \cdot R_\infty$. In flat space-time $\delta = \theta$ while here $\delta < \theta$. The maximum collatitude visible to an observer at infinity corresponds to $\delta = \pi/2$, i.e., $\theta_{max} = \theta(x = 1)$, and the star appears as a disc of radius R_∞ . For a given star mass, R_∞ is minimal at $R = (3/2)R_S$, with $R_S = 2GM/c^2 = 2.95 \text{ km } M/M_\odot$ the star’s Schwarzschild radius, and is $R_\infty^{min} = (3\sqrt{3}/2) R_S \simeq 2.6R_S$ (thus, a $1.4 M_\odot$ neutron star radius cannot appear smaller than 10.74 km, for an actual value of 4.134 km). We show in Fig. 3 the value of the maximum lensing angle θ_{max} as a function of the star’s radius R . θ_{max} reaches 180° at $R/R_S \simeq 1.76$, 360° at $R/R_S \simeq 1.5091$, and goes to infinity when R/R_S tends to 1.5 ($r_\gamma = 1.5R_S$ is the so-called ‘photon radius’ at which a photon can be in a circular Keplerian orbit around the star, if $R < r_\gamma$).

To obtain the flux received by a detector the only change compared to the development of § 4.1. is in Equ. 10 where $\cos \theta$ becomes $\cos \delta$ (the surface element d^2A remains $R^2 \sin \theta d\theta d\phi$ by definition of the Schwarzschild coordinates) and in the calculation of the detector’s solid angle $d\Omega_p$. The latter can be seen to be (see, e.g., Appendix I in Pechenick *et al.* 1983):

$$d\Omega_p = \frac{x \, dx}{\cos \delta \sin \theta \, d\theta} \left[\frac{A(E)}{D^2} \right]. \quad (19)$$

The term $x \, dx$ in Equ. 13 is $\cos \theta \sin \theta \, d\theta$ which is exactly canceled by the term $\cos \delta \sin \theta \, d\theta$ of Equ. 19 (since $\cos \theta \rightarrow \cos \delta$ in Equ. 10). The photon flux $\mathcal{N}(E_\infty)$ is thus still given by Equ. 15 and 13 but now with $x \equiv \sin \delta$.

The actual sizes of neutron stars are unknown and this lensing effect rises the hope of imposing some constraints on them. Theoretical predictions, for a $1.4 M_{\odot}$ star, range from 6.5 km up to a maximum of 14 km. The smallest value (6.5 km) appears in models with either a kaon condensate (Thorsson, Prakash & Lattimer 1994) or hyperons (Pandharipande 1971) and the largest values (14 km) are obtained in models with only nucleons and developed within the mean field theory. For models with only nucleons, the classical equation of state (EOS) of Friedman & Pandharipande (1981) and its improved versions by Wiringa, Fiks & Fabrocini (1988) give radii between 10.5 and 11.5 km at $1.4 M_{\odot}$. Very low mass neutron stars have much larger radii but, when restricting ourselves to masses around $1.4 M_{\odot}$, 14 km should be considered as an upper limit in the models.

4.3. The detector's response

The number of counts in the detector's output channel $\#i$, $Cts(i)$, is obtained from $\mathcal{N}(E_\infty)$ with the detector's response matrix (r_{ij}):

$$Cts(i) = \Delta t \sum_j r_{ij} \mathcal{N}(E_j) \delta E_j. \quad (20)$$

For *ROSAT*'s PSPC there are 256 output channels ($i = 1, \dots, 256 = I$, but channels 1 - 7 have a zero effective area) and the incoming flux is split in 729 energy bands δE_j ($j = 1, \dots, 729 = J$). Δt is the observing time. The r_{ij} have dimension $[\text{cm}^{-2}]$ and the detector's effective area at energy E_j is $A(E_j) = \sum_i r_{ij}$ while the detector's effective area for channel i is $A_i = \sum_j r_{ij}$. In all our calculations we use the 1992 March 19 release of the PSPC's response matrix. A perfect resolution detector would have $I = J$ and $r_{ij} = \delta_{ij} \cdot A(E_i)$.

4.4. Numerical method

Given the star's mass M and radius R we define the magnetic dipole's strength B_p and inclination angle α with respect to the rotation axis. The magnetic field is calculated at each point of a fixed grid on the star's surface (about one point per square degree) and, given the interior temperature T_b , the surface temperature is calculated on this grid using Equ. 6 and 7. We then define a mobile grid on the surface, which covers the part of the star visible to the observer taking into account lensing, with usually one point per 3^2 square degrees or one point per square degree for cases of very strong lensing. Given the observer's orientation ζ with respect to the rotation axis, the mobile grid is rotated by steps of 6 degrees, at each step the temperature is calculated on this grid by interpolating from the values previously calculated on the fixed grid and the averaged distribution function (Equ. 13) is calculated, usually for about one hundred values of the photon's energy E . Given the observer's distance D and the hydrogen column density N_H , the fluxes $\mathcal{N}(E)$ are calculated (Equ. 15) and then passed through the detector's response matrix (Equ. 20) to give the counts which can be directly compared with the data.

5. RESULTS

5.1. Surface Temperature Distributions

With the method of § 3.2. we can now calculate surface temperature distributions for given magnetic field configurations. Figure 4 shows a typical example for a dipolar surface field, other dipole strengths and internal temperatures giving similar results. Figures 5a) and b) give the percentage of the star’s area with temperature inferior to a given value for various field intensities B_p and internal temperatures T_b . For a given T_b , increasing B_p results in a smaller proportion of the surface having a temperature close to the minimal temperature T_{min} , while for a given B_p the same effect is obtained by decreasing T_b . Having the surface temperature distribution $T_s(\theta, \phi)$ we can calculate the effective temperature $T_e = \langle T_s^4(\theta, \phi) \rangle^{1/4}$ ($\langle X \rangle$ means surface average of X) and the average temperature $T_a = \langle T_s(\theta, \phi) \rangle$ which will be used below. From Figures 4 and 5 one sees that most of the surface is at a temperature close to the maximal temperature T_{max} (reached around the magnetic poles), but that the temperature drops to very low values on a small portion of the star.

5.2. Spectra

In this paper we use blackbody emission at each point on the surface, at the local temperature: our spectra are thus composite blackbody spectra. The effect of the non uniformity of the surface temperature on the spectrum turns out to be relatively small, the resulting spectra being very close to Planck spectra. Figure 6 shows a typical example, the same dipolar field as in Figure 4: one sees that the blackbody spectrum at the effective temperature (dashed curves) is a reasonably good approximation to the ‘exact’ spectrum (continuous curves), particularly when the detector resolution is taken into account where both spectra are almost identical below 0.5 keV. Since a second spectral component is present above 0.5 keV, spectral fits to estimate the surface temperature are mostly sensitive to the soft band below 0.5 keV and consequently, *as far as blackbody fits are concerned, single temperature fits are practically as good as our composite model to determine the effective temperature.* Changing the field configuration and the observer’s conditions (orientation, distance and column density) makes little difference. This result was already mentioned by Greenstein & Hartke (1983). The excess above 0.5 keV of the composite

spectrum compared to the blackbody spectrum at T_e will though change the value of the parameters used to model the hard component.

Phase dependent spectra are very close to the phase integrated spectrum, the difference being often below the detection limit with reasonable exposure times. Again, changing the dipole's strength and orientation, or the observer's conditions, makes little difference. If spectra from magnetic atmosphere models were used the results may be different since, when the temperature (and/or the surface field strength) varies, the shape of the spectrum changes while the blackbody spectrum's shape is invariant. Gravitational lensing has obviously no effect on the phase integrated spectrum, but will affect phase resolved spectra and make them even closer to the phase integrated spectrum. However light curves are more appropriate to study this effect.

5.3. Light curves

The properties of the observed light curves (see Table 1) that one should keep in mind here are the presence of one or two peaks, the phase of the peak(s) and the pulsed fraction, as well as their dependence on the photon energy. We define the pulsed fraction as:

$$Pf(i) = \frac{\frac{1}{2}(Cts_{max} - Cts_{min})}{Cts_{mean}} \quad (21)$$

where Cts_{max} , Cts_{min} and Cts_{mean} are, respectively, the maximal, minimal, and mean count rates in a given detector channel ($i=8, \dots, 256$ for *ROSAT*'s PSPC) The observed pulsed fractions are of course delicate to measure and can only be defined for a range of channels, $Pf(i_1 - i_2)$.

A surface dipolar field with two oppositely located warm regions on the star's surface gives light curves with one or two peaks, and singleness of the peak imply that the angle α between the magnetic dipole and the rotation axis and the angle ζ between the observer's direction and the rotation axis must satisfy, in flat space-time,

$$\alpha + \zeta < 90^0 \quad (22)$$

to assure that only one magnetic pole is ever seen. Gravitational lensing will impose a more stringent condition but, on the other side, the statistical uncertainty in the observed counts makes that low amplitude peaks in the light-curve cannot be recognized. We show in Figure 7 seven examples of light curves with $\alpha = \zeta$ and the corresponding pulsed fractions.

We find, for single peak configurations, that the maximum pulsed fraction is obtained when $\alpha \sim \zeta \sim 45^\circ$, which is obvious from geometrical reasons. If $\alpha \sim \zeta > 45^\circ$ the pulsed fraction is comparable or slightly lower than at 45° and a second peak appears. An important, simple, fact seen in *all* cases we have considered, from which only the most representative are presented in this paper, is that *the phase of the peak(s) in the light curve is independent of the photon energy in the whole range 0.08 - 2.5 keV*, as can be seen for example in Fig. 7.

The lower the effective temperature T_e the higher the pulsed fraction Pf which comes from the fact that at lower temperatures the difference between T_{max} and T_{min} is larger (see Fig. 1). A surprising result is that the highest magnetic fields do not give the largest pulsed fractions. As shown in Fig. 5b, a larger portion of the surface is at low temperature at field strengths around $3 \cdot 10^{11}$ G than at higher fields: it is thus at $B_p \sim 3 \cdot 10^{11} - 10^{12}$ G that we obtain the highest pulsed fractions, and stronger fields have a pulsed fraction slightly lower.

A general characteristic of pulsed fractions with dipolar fields and blackbody emission is that they rise with photon energy, slowly at low and high energy but with an intermediate region of faster increase whose exact location depends on the effective temperature but is always around 0.5 keV. The presence of this steeper rise around 0.5 keV is actually a product of the PSPC's response characteristics as can be seen from Fig. 8 where the pulsed fraction of the incoming flux (as it would be recorded by a detector with perfect energy resolution) is compared with PSPC-detected pulsed fractions. This feature will thus certainly be present even for more complex surface temperature distributions.

If the detector has a very good energy resolution Pf is independent of interstellar absorption since its effect is just to reduce the incoming flux at energy E by a factor $\exp(-N_H \sigma(E))$ which drops out when calculating Pf . However, when dealing with a detector like *ROSAT's* PSPC, the finite energy resolution does affect the pulsed fraction by mixing in the same output channel photons with different energies and thus different absorptions. Since $\sigma(E) \sim E^{-3}$, the net effect of interstellar absorption is to suppress the soft photons compared to the harder ones and when increasing N_H the lowest PSPC's channels become proportionally more and more contaminated by hard photons. The result is a rise of the pulsed fraction in these lowest channels (Figure 8). However, very large values of N_H are required to obtain a significant rise in Pf , and such high values are clearly excluded in the cases of the four pulsars we consider: they would dramatically reduce the flux at low energy, much below anything observed.

The last point we consider is the effect of gravitational lensing. The effect on the spectrum is very small (at least for dipolar fields) and at the limit of observability due to the low count rates, but when adding the output of many channels into light curves their flattening can be clearly seen: *the pulsed fraction is strongly dependent on the size*

of the star, besides its much weaker dependence on the dipole’s strength and the effective temperature. We show in Figure 9 a sequence of light curves where the star’s radius is decreased from ∞ (i.e., no lensing effect) down to 6.25 km (i.e., $R/R_S = 1.51$), the star’s mass being kept at $1.4 M_\odot$. The corresponding pulsed fractions are shown in Fig. 10. The dipole and the observer are at 90° to the rotation axis and the dipole strength and interior temperature are chosen to maximalize the pulsations according to the above discussion. One immediately sees the dramatic effect of lensing which reduces Pf from about 25% (below 0.5 keV) in flat space-time to a half of this at a radius of 18 km (an unrealistically large value for a $1.4 M_\odot$ neutron star) and to a tenth of this at a radius of 10 km. As another example, we took a series of 6 neutron stars with masses and radii of: ($1.0 M_\odot$, 11.21 km), ($1.2 M_\odot$, 11.08 km), ($1.4 M_\odot$, 10.89 km), ($1.6 M_\odot$, 10.55 km) and ($1.8 M_\odot$, 9.76 km) (these radii correspond to the EOS of Friedman & Pandharipande 1981). With an internal temperature of 5×10^7 K, a dipole strength of 3×10^{12} G, and $\zeta = \alpha = 90^\circ$, we obtained pulsed fractions, in the energy band 0.08-0.5 keV, of 12%, 8%, 4%, 1%, and 1% respectively. There is also a tricky effect at radii between 8.85 km and 7.3 km: the peak of the light curve is 90° off-phase with respect to larger or smaller radii. At large radii ($R > 8.85$ km) the peaks correspond to one of the magnetic poles being seen face-on and when R decreases more of the cool region in the magnetic equator is visible at this phase, thus reducing the amplitude of the pulsations. When $7.3 < R < 8.85$ km, the flux with the poles face-on is now lower than when they are seen sideway (phases 0.25 and 0.75) where both warm polar regions are wholly seen because of the strong lensing; at still smaller radii, the second pole becomes visible in the face-on configurations and the peak is back at phases 0 and 0.5. This latter effect of increase of the pulsed fraction at small radii when the whole surface of the star is visible and a hot region passes on the antipode with respect to the observer, ‘gravitational beaming’, has already been described by Pechenick *et al.* (1983) and the off-phasing of the peak at slightly larger radii can also be seen in their figures. Orienting the magnetic dipole and the observer at 45° to the rotation axis, $\alpha = \zeta = 45^\circ$, gives very similar results: the light curves have the shapes shown in Fig. 7, the pulsed fractions are observationally indistinguishable from the ones of Fig. 10 (for the same temperature distribution) and the off-phasing of the peaks also happens at practically the same star’s sizes. If we define a phase dependent effective temperature T_e^Φ from the average of $T_s^4(\theta, \phi) \cdot \cos \delta$ over the part of the star seen by the observer, i.e., an effective temperature that fits the phase dependent spectra, then, for the cases of Fig. 9, T_e^Φ at the maximum exceeds T_e^Φ at the minimum by about 13% when there is no lensing, down to 6% at $R = 18$ km, 4.2% at $R = 14$ km and 0.9% at $R = 10$ km.

6. DISCUSSION

The magnetic envelope calculations we use to model the surface temperature distribution tell us that the temperature of the warmer regions, where the field is radial ($\Theta_B \sim 0$), is several times higher than the temperature of the regions where the magnetic field is tangential ($\Theta_B \sim 90^\circ$) as shown in Fig. 1. There are thus very large temperature differences on the surface but the resulting effective temperature seen by an observer at infinity, who averages over the part of the star he sees, varies little during the star's rotation. Variations are of the order of 5-10% for observed pulsed fraction of 10-30% below 0.5 keV and the observed spectrum varies thus little with the rotational phase. Magnetic effects on the emitted spectrum by themselves are important and it is possible that when included in our model they may produce more significant and interesting variations in the observed spectra. These will hopefully be included in future work and for the time being we will concentrate on the light curves.

The first noticeable characteristic of the observed light curves for the four pulsars we study is their substantial pulsed fraction: the results of Fig. 10 show that these values, between 10 – 30% below 0.5 keV, could be obtained with simple dipolar fields. However the radii required, to avoid the flattening from gravitational lensing, are larger than the present theoretical predictions if the neutron star mass is assumed to be $1.4 M_\odot$. Models with only nucleons in the core give the largest radii, and the most sophisticated models (Wiringa *et al.* 1988; M  ther, Prakash & Ainsworth 1987) give radii between 10 - 12.5 km while other predictions barely reach 14 km (Glendenning 1985 e.g.). Models with meson condensates, hyperons or quarks give smaller radii (Thorsson *et al.* 1994, Glendenning 1985, Glendenning 1992) For any of these values, the pulsed fractions in the energy range 0.08 - 0.5 keV, for whatever values of the parameters (B_p , T_b , α and ζ), are below 10%. Analyses of the Vela pulsar glitches do favor large radii (Link, Epstein & Van Riper 1992; Alpar *et al.* 1993) but values above 15 km (for a $1.4 M_\odot$ neutron star) needed to give high enough Pf are not supported to date by any neutron star model. Older calculations of neutron stars with solid neutron cores did give radii of the order of 16 km (Pandharipande & Smith 1975), but the solidification of neutrons in neutron stars is not considered anymore as realistic. Taking neutron stars of lower masses raises the pulsed fraction, e.g., up to 12% for a $1.0 M_\odot$ star with radius of 11.2 km as seen in § 5.3. using a realistic EOS, but still below 10% at masses above $1.2 M_\odot$. So considering stars of mass lower than $1.4 M_\odot$ is not sufficient to obtain the high observed pulsed fractions unless a very stiff EOS is used. However, the values obtained are not much below the observed ones unless the star's radius is small.

Spectra from magnetized hydrogen atmospheres give by themselves pulsed fractions of the order of 10% (Pavlov *et al.* 1994) for a dipolar field with a uniform surface temperature

and *no* lensing: when used with the appropriate temperature distributions it is reasonable to expect that they will increase Pf compared to the blackbody case, but the effect of the magnetic field considered in this paper will probably dominate (we obtain a 25% modulation without lensing). Using non magnetic hydrogen atmosphere spectra (Page, Zavlin, Pavlov & Shibano, work in progress) one can get higher Pf , between 10-20% for standard masses and radii; the increase, compared to blackbody spectra, being due to the slight radial beaming produced by the limb darkening effect.

Our model shows that, for a fixed magnetic field configuration, the difference between the maximum and minimum surface temperature and hence the observed pulsed fraction increases with decreasing temperature. It may be interesting to notice (see Table 1) that this trend is present within our very limited sample of four objects. It may just be a coincidence or may indicate the occurrence of a general pattern of field evolution in which pulsars after a few thousands of years develop similar surface field configurations.

In the cases of PSR 0833-45, 0656+14 and 1055-52 the observed pulsed fractions are weakly energy dependent below 0.5 keV, which is almost what we obtain. However, the slight rise in Pf in our results may be important since this does not correspond exactly to the observations: the observed pulsed fraction of PSR 1055-52 seems to be slightly decreasing with increasing energy (below 0.5 keV). In the case of Geminga, though, there is a significant decrease of Pf in the band 0.28 – 0.5 keV compared to its value below 0.28 keV: *this feature is absolutely impossible to reproduce in our models* (we doubt that more complex field configurations will alter this conclusion). This may be evidence for the inadequacy of blackbody emission and the result of genuine atmospheric magnetic effects on the emitted spectrum. In case of a very high column density (see Fig. 8) we do obtain a decrease of Pf at low energy but it is much smaller than what is observed in Geminga and the column densities required, $N_H > 10^{21} \text{cm}^{-2}$, are at least an order of magnitude too high.

Even if we can somewhat reproduce the observed pulsed fractions we do not score well on the shape of the light curves in the three cases where they are single peaked (PSR 0656+14, 0630+178 and 1055-52). A single-peaked light curve with a dipolar magnetic field restricts the geometry to $\alpha + \zeta \lesssim 90^\circ$ and the resulting theoretical light curves have a long flat minimum and relatively narrow peaks (Fig. 7): this is opposite to the observations where the peaks are broad and the light curves are above their mean more than 50% of the time. The use of magnetic spectra will change the shape of the light curves but probably in the ‘wrong’ direction: emission is beamed along the field and one can expect that the peaks will be narrower. We can safely conclude from this that the surface magnetic field of these three stars is certainly not dipolar.

A simple way out of this problem is the addition of a small quadrupolar component

(Page 1994b) to broaden the peaks, keeping $\alpha + \zeta \lesssim 90^\circ$. That may be a reasonable solution for PSR 0656+14 but for PSR 1055-52 and 0630+178 the situation is probably different. Phenomenological description of the radio emission indicates (see Table 1) that $\alpha \sim \zeta \sim 30^\circ$ or 8.2° for PSR 0656+14: if we accept this geometry then only one polar region is seen and the broadening of the soft X-ray light curve's peak should be achieved with an alteration of the dipolar field. However the small value of α and ζ estimated by Lyne & Manchester (1988), 8.2° , yields pulsed fractions of at most 1% (Fig. 7) with a dipolar field (no matter what the strength of the dipole or the temperature is); magnetic effects on the emitted spectrum will doubtly be sufficient to raise this to the observed 14%. The $30^\circ - 35^\circ$ inclination of Rankin (1993) or Malov (1990) give $Pf \sim 8 - 10\%$ and could work once magnetic spectra are used. A quadrupole component added to the dipole can also easily increase Pf though (Page 1994b).

In the case of PSR 1055-52 and 0630+178 interpretation of the the radio and γ -ray emission, respectively, indicate that $\alpha \sim \zeta \sim 90^\circ$. A dipolar surface field will definitely give two peaks: if the dipolar component is orthogonal to the rotation axis there obviously must be *strong* higher order multipolar components, as already mentioned by Halpern & Ruderman (1993). This case will be considered in detail in a forthcoming paper (Page 1994b). The alternative interpretation of PSR 1055-52 as being an almost aligned rotator (Malov 1990) was supported according to Malov (1989) by the absence of pulsation in the X-ray band in the *Einstein* observation (Cheng & Helfand, 1983), an argument invalidated by the *ROSAT* detection of pulsations. With $\alpha \sim \zeta \sim 30^\circ$ (Malov 1990) we obtain a pulsed fraction just below 10% (Fig. 7) in the most optimistic case ($B_p = 10^{12}$ G, low temperature and large radius of 16 km). Smaller radii will reduce Pf well below the observed 11% but, on the other hand, magnetic effect on the emitted spectrum will certainly be sufficient to give 11%. Thus the inclination angles proposed by Malov (1990) are probably able to give pulsed fractions as observed, but the asymmetric shape of the light curve again requires a non dipolar surface field.

The light curves of PSR 0833-45 (Vela) are more delicate to interpret. The two *ROSAT* observations, separated by eight months, show two somewhat different light curves where several narrow subpeaks have moved in phase and amplitude. By considering the two observations together one can distinguish two peaks, the larger one about 210° wide and the smaller one about 100° wide with an amplitude about one third the amplitude of the large peak. However the dip which separates the small peak may be due to fluctuations and this small peak inexistent. An orthogonal configuration, $\alpha \sim \zeta \sim 90^\circ$, as suggested by analysis of the radio pulse, with a surface dipolar field, gives two soft X-ray peaks but the large difference in amplitude between the two observed peaks imply a distortion of the field from the pure dipole. An orientation with $\alpha \sim \zeta \sim 60^\circ - 70^\circ$ (as preferred, e.g., in outer

gap models of its γ -ray emission, Romani & Yadigaroglu 1994) would give better results, i.e., peaks of different amplitudes, but the peaks are definitely narrower than observed (and again inclusion of magnetic atmosphere effects will make the peaks still narrower). If the small peak is rejected then we are in the same situation as with PSR 0630+178 and 1055-52: there must be strong quadrupolar, or higher order, components in the magnetic field.

Our discussion assumed that the contamination of the soft X-ray emission by the hard component is negligible: this is true when blackbody emission is used for both components, and also when magnetic atmosphere effects are included in the soft component (Meyer *et al.* 1994). Should the hard component contribute significantly to the soft band emission our conclusion may be affected.

Several models of neutron stars with a pion or kaon condensate give very small radii (Maxwell & Weise 1976; Thorsson *et al.* 1994) and thus lead to very small modulations in the light curves, in sharp contradistinction to what is observed. We thus have a new tool to test these models, but one should not consider that our present results rule them out so far: surface magnetic field configurations more complex than the simple dipoles considered here, as well as magnetic effects on the emitted spectrum, may lead to stronger pulsations and the question needs more study (Page 1994b). If neutron stars are actually as small as these models with meson condensates claim, the off-phasing of the light curves with respect to the viewing (Fig. 9) at radii between 7.5 - 8.5 km must induce us to use extreme care in relating the soft X-ray peak phases with pulsations observed at other wavelengths. This range of radii includes the calculated values for a $1.4 M_{\odot}$ neutron star in many models.

7. CONCLUSIONS

The simple model presented here, with dipolar fields, shows several features similar to the observed ones but with significant shortcomings. We obtain pulsed fractions which are lower than the observed ones, unless very large radii or very low masses are assumed. The shape of the light curves do not match the observations, indicating the presence of deviations from a purely dipolar field, the strength of the required correction depending on the assumed geometry and the size of the star. One can, however, reasonably expect that more complicated field structure will be able to reproduce the observed pulsed fractions and the shapes of the light curves: there is probably no need to invoke external heating of the surface and/or magnetospheric absorption (see Introduction) to reproduce the data, but this does not mean that these processes are not present. ‘Energy dependent pulse shapes and phases are trying to tell us the whole story; we have to interpret them’ (Ögelman 1993),

but deciphering the story will not be easy. A complete model will have to consider complex surface fields and also include the magnetic effects in the atmosphere.

I am grateful to J. H. Applegate, J. P. Halpern, Y. Shibano and G. G. Pavlov for discussions, as well as A. Sarmiento, A. Serrano and E. Vazquez. My interest in this problem was triggered by an unpublished talk of S. Tsuruta (U. of Oklahoma, March 1991). This work was supported by a HEA-NASA grant NAGW 3075 at Columbia and by a DGAPA grant IN104092 at the UNAM. This is contribution number 350 of the IA-UNAM.

Table 1. Some observational properties ^a

	PSR 0833-45 (Vela)	PSR 0656+14	PSR 0630+178 (Geminga)	PSR 1055-52
P (msec)	89	385	237	197
τ (yrs)	1.2×10^4	1×10^5	3×10^5	5×10^5
T_e^{BB} (K) ^b	$1.5 - 1.6 \times 10^6$	$8.6 - 9.4 \times 10^5$	$4.2 - 6.2 \times 10^5$	$6.3 - 7.5 \times 10^5$
N_H^{BB} (cm ⁻²) ^b	$0.1 - 1.5 \times 10^{20}$	$0.8 - 1.2 \times 10^{20}$	$1 - 2 \times 10^{20}$	$2.0 - 4.5 \times 10^{20}$
Soft component ^b	$Pf \sim 11\%$ one or two peaks (?)	$Pf \sim 14\%$ one peak	$Pf \sim \begin{cases} 33\% (0.08 - 0.28keV) \\ 10\% (0.28 - 0.5keV) \end{cases}$ one peak	$Pf \sim 11\%$ one peak
Hard component ^b	Unpulsed	?	$Pf \sim 35\%$	$Pf \sim 20 \rightarrow 80\%$
$\phi_S - \phi_H$ (deg) ^b	n/a	n/a	~ 105	~ 120
Radio pulsar	Yes (one pulse)	Yes (one pulse)	No	Yes (two pulses)
Optical counterpart	Yes (pulsed)	Yes (proposed) ^c	Yes (confirmed) ^d	None to date
γ -ray pulsar	Yes (two pulses)	No	Yes (two pulses)	Yes (one pulse) ^e
B_p (G)	6.8×10^{12}	8.8×10^{12}	3.2×10^{12}	2.2×10^{12}
α (deg) ^f	$\begin{cases} \text{LM : 90} \\ \text{R : 90} \\ \text{M : 35} \end{cases}$	$\begin{cases} \text{LM : 8.2} \\ \text{R30} \\ \text{M35} \end{cases}$	~ 90	$\begin{cases} \text{LM : 74.7} \\ \text{R90} \\ \text{M30} \end{cases}$
ζ (deg) ^f	$\begin{cases} \text{LM : 83} \\ \text{R : 78} \end{cases}$	$\begin{cases} \text{LM : 8.2} \\ \text{R : 30} \\ \text{M : 35} \end{cases}$	~ 90	$\begin{cases} \text{LM : 66.8} \\ \text{R : 90} \\ \text{M : 30} \end{cases}$

^aThe rows list respectively: the period P , spin down age $\tau = P/2\dot{P}$, effective temperature from blackbody fit T_e^{BB} and the associated hydrogen column density N_H^{BB} , pulsed fraction Pf and number of peaks of the soft X-ray component, pulsed fraction Pf of the hard X-ray component, phase difference between the peaks of the soft and hard X-ray components, detections at radio, optical and γ -ray wavelengths, the dipolar field strength (Equ.1) and the estimated angles between the magnetic dipole and the rotation axis (α) and between the observer's direction and the rotation axis (ζ).

^bValues are from Ögelman *et al.* 1993 for Vela, Finley *et al.* 1992 for 0656+14, Halpern *et al.* 1993 for Geminga and Ögelman *et al.* 1993 for 1055-52.

^cCaraveo *et al.* 1994

^dBignami *et al.* 1993

^eFierro *et al.* 1993

^fValues are from Lyne *et al.* 1988 (LM), Rankin 1993 (R), Malov 1990 (M) and for Geminga: Halpern *et al.* 1993.

REFERENCES

- Alpar, M. A., Chau, H. F., Cheng, K. S. & Pines, D. 1993, *ApJ*, 409, 345
- Anderson, S. B., Córdoba, F. A., Pavlov, G. G., Robinson, C. R. & Thompson, Jr, R. J. 1993, *ApJ*, 414, 867
- Becker, W. & Aschenbach, B. 1993, in *Lives of the Neutron Stars*, eds. A. Alpar, Ü Kızıloğlu, & J. van Paradijs (Dordrecht: Kluwer Academic Publishers), in press
- Bignami, G. F., Caraveo, P. A. & Mereghetti, S. 1993, *Nature*, 361, 704
- Bignami, G. F., Caraveo, P. A. & Lamb, R. C. 1983, *ApJ*, 272, L9
- Bowyer, S., Byram, E. T., Chubb, T. A. & Friedman, H. 1964, *Nature*, 201, 1307
- Brinkmann, W. 1980, *A&A*, 82, 352
- Brinkmann, W. & Ögelman, H. 1987, *A&A*, 182, 71
- Brown, L. E. & Hartmann, D. H. 1993, *Ap&SS*, 209, 285
- Caraveo, P. A., Bignami, G. F. & Mereghetti S. 1994, *ApJ*, 422, L87
- Caraveo, P. A., Bignami, G. F., Giommi, P., Mereghetti, S. & Paul, J. A. 1984, *Nature*, 310, 481
- Chen, H.-H., Ruderman, M. & Sutherland, P. G. 1974, *ApJ*, 191, 473
- Cheng, A. F. & Helfand, D. J. 1983, *ApJ*, 271, 271
- Córdoba, F. A., Hjellming, R. M., Mason, K. O. & Middleditch, J. 1989, *ApJ*, 345, 451
- Fierro, J. M. *et al.* 1993, *ApJ*, 413, L27
- Finley, J. P., Ögelman, H. & Kızıloğlu, Ü 1992, *ApJ*, 394, L21
- Friedman, B. & Pandharipande, V. R. 1981, *Nucl. Phys.*, A361, 502
- Ginzburg, V. L. & Ozernoy, L. M. 1964, *Zh. Eksp. Theor. Fiz.*, 47, 1030 (1965, *JETP*, 20, 689)
- Glendenning, N. K. 1985, *ApJ*, 293, 470
- Glendenning, N. K. 1992, *Phys. Rev.*, D46, 1274
- Greenstein, G. & Hartke, G. J. 1983, *ApJ*, 271, 283
- Gudmundsson, E. H., Pethick, C. J. & Epstein, R. I. 1982, *ApJ*, 259, L19
- Gudmundsson, E. H., Pethick, C. J. & Epstein, R. I. 1983, *ApJ*, 272, 286
- Halpern, J. P. and Holt, S. S. 1992, *Nature*, 357, 222

- Halpern, J. P. & Ruderman, M. 1993, *ApJ*, 415, 286
- Halpern, J. P. & Tytler, D. 1988, *ApJ*, 330, 201
- Harding, A. K., Ozernoy, L. M. & Usov, V. V. 1993, *MNRAS*, 265, 921
- Harnden, F. R., Grant, P. D., Seward, F. D. & Kahn, S. M. 1985, *ApJ*, 299, 828
- Hernquist, L. 1985, *MNRAS*, 213, 313
- Hernquist, L. & Applegate, J. H. 1984, *ApJ*, 287, 244
- Jones, P. B. 1986, *MNRAS*, 218, 477
- Link, B., Epstein, R. I. & Van Riper, K. A. 1992, *Nature*, 359, 616
- Lyne, A. G. & Manchester, R. N. 1988, *MNRAS*, 234, 477
- Ma, Y., Lu, T., Yu, K. N. & Young, E. C. M. 1993, *Ap&SS*, 201, 113
- Malov, I. F. 1989, *Pis'ma Astron. Zh.*, 15, 455 (*Sov. Astron. Lett.*, 15, 196)
- Malov, I. F. 1990, *Astron. Zh.*, 67, 377 (*Sov. Astron.*, 34, 189)
- Maxwell, O. & Weise, W. 1976, *Phys. Lett.*, B62, 159
- Meyer, R. D., Pavlov, G. G. & Mészáros, P. 1994, *ApJ*, in press (Sept. 20 issue)
- Miller, M. C. & Hamilton, R. J. 1993, *ApJ*, 411, 298
- Morrison, R. & McCammon, D. 1983, *ApJ*, 270, 119
- Müther, H., Prakash, M. & Ainsworth, T. L. 1987, *Phys. Lett.*, B199, 469
- Nomoto, K. & Tsuruta, S. 1986, *ApJ*, 305, L19
- Nomoto, K. & Tsuruta, S. 1987, *ApJ*, 312, 711
- Ögelman, H., 1991, in *Neutron Stars: Theory and Observation*, eds. J. Ventura, & D. Pines (Dordrecht: Kluwer Academic Publishers), 87
- Ögelman, H., 1993, in *Lives of the Neutron Stars*, eds. A. Alpar, Ü Kiziloğlu, & J. van Paradijs (Dordrecht: Kluwer Academic Publishers), in press
- Ögelman, H. & Finley J. P. 1993, *ApJ*, 413, L31
- Ögelman, H., Finley, J. P. & Zimmermann, H.-U. 1993, *Nature*, 361, 136
- Ögelman, H. & Zimmermann, H.-U. 1989, *A&A*, 214, 179
- Page, D. 1994a, *ApJ*, 428, 250
- Page, D. 1994b, 'Surface Temperature of a magnetized Neutron Star and Interpretation of the *ROSAT* Data. II. Complex magnetic Fields', in preparation
- Page, D. & Applegate, J. H. 1992, *ApJ*, 394, L17

- Pandharipande, V. R. 1971, Nucl. Phys., A178, 123
- Pandharipande, V. R. & Smith, R. A. 1975, Nucl. Phys., A237, 507
- Pavlov, G. G., Shibarov, Yu. A., Zavlin, V. E. & Meyer, R. D. 1994, in *Lives of the Neutron Stars*, eds. A. Alpar, Ü Kiziloğlu, & J. van Paradijs (Dordrecht: Kluwer Academic Publishers), in press
- Pechenick, K. R., Ftaclas, C. & Cohen, J. M. 1983, ApJ, 274, 846
- Rankin, J. M. 1993, ApJS, 85, 145
- Romani, R. W. 1987, ApJ, 313, 718
- Romani, R. W. & Yadigaroglu, I.-A. 1994, submitted to ApJ
- Ruderman, M. 1974, in IAU Symposium 53, *Physics of Dense Matter*, ed. C. J. Hansen (Dordrecht: D. Reidel Publishing Company), 117
- Schaaf, M. E. 1990a, A&A, 227, 61
- Schaaf, M. E. 1990b, A&A, 235, 499
- Shibarov, Yu. A., Zavlin, V. E., Pavlov, G. G. & Ventura, J. 1992, A&A, 266, 313
- Seward, F. D. & Wang, Z.-R. 1988, ApJ, 332, 199
- Thorsson, V., Prakash, M. & Lattimer, J. M. 1994, Nucl. Phys., A572, 693
- Van Riper, K.A. 1988, ApJ, 329, 339
- Wiringa, R. B., Fiks, V. & Fabrocini, A. 1988, Phys. Rev., C38, 1010
- Yakovlev, D. G. & Kaminker, A. D. 1994, in IAU Colloquium 147, *Equation of State in Astrophysics*, eds G. Chabrier & E. Schatzman (Cambridge: Cambridge University Press), in press

Fig. 1.— $T_b - T_s$ relationship for transport parallel and perpendicular to the field at various field strengths. T_b is the temperature at the bottom of the envelope whose density is fixed at $10^{10} \text{ gm cm}^{-3}$ and T_s is the ‘surface’ or effective temperature. The dependence on the star’s mass and radius is entirely contained in the scaling factor $g_s^{1/4}$. The continuous line gives the non magnetic relationship. The high values of T_s correspond to a radial magnetic field (parallel transport) and are taken from Hernquist (1985) while the low T_s values correspond to a field tangential to the surface (orthogonal transport) and are from Schaaf (1990a). The values of T_s lower than $10^{5.5}$ K are linear extrapolations of the higher values and must be considered only as illustrative (see text).

Fig. 2.— Geometry of gravitational lensing.

Fig. 3.— Maximum lensing angle vs. neutron star’s radius for a $1.4 M_\odot$ star and vs. radius in unit of the Schwarzschild radius $R_S = 2GM/c^2 = 2.95 \text{ km } M/M_\odot$.

Fig. 4.— Surface temperature distribution with a dipolar magnetic field with field strength $B_p = 3 \cdot 10^{12}$ G at the poles (marked by stars) and an internal temperature of $6 \cdot 10^7$ K ($g_{s14} = 1$). The effective temperature is $6.27 \cdot 10^5$ K and the average temperature is $5.8 \cdot 10^5$ K. The representation is an area preserving mapping.

Fig. 5.— Percentage of the star’s area with temperature lower than a given value for dipolar fields. T_{min} and T_{max} are the minimum and maximum temperatures on the surface which can be read from Figure 1.

a) $B_p = 3 \cdot 10^{12}$ G with four different interior temperatures: $3 \cdot 10^7$ K (dash-dot), $6 \cdot 10^7$ K (dash-triple dot), 10^8 K (continuous) and $3 \cdot 10^8$ K (dash).

b) $T_{int} = T_b = 10^8$ K with five different dipole strengths: $3 \cdot 10^{11}$ G (dash-dot), 10^{12} G (dash-triple dot), $3 \cdot 10^{12}$ G (continuous), $6 \cdot 10^{12}$ G (dash) and 10^{13} G (dot).

These curves are independent of the mass and radius of the star.

Fig. 6.— Incoming (a) and detected (b) spectra for the temperature distribution shown in Figure 4. ($D = 250$ pc, $N_H = 10^{20} \text{ cm}^{-2}$ and $\alpha = \zeta = 90^\circ$). The continuous lines show the total composite spectrum while the dotted lines are a blackbody spectrum at the average temperature and the dashed lines a blackbody spectrum at the effective temperature. The incoming spectra (a) are $\mathcal{N}(E_\infty)$ and the detected spectra (b) are $Cts(i)/\Delta t/\delta E$, i.e., the incoming spectra passed through the response matrix.

Fig. 7.— Light curves (left) and pulsed fractions (right) for seven orientations of the observer and magnetic dipole: $\alpha = \zeta = 8^\circ, 15^\circ, 30^\circ, 45^\circ, 60^\circ, 75^\circ$ and 90° . In all cases the field is dipolar with strength $B_p = 10^{12}$ G and the internal temperature $T_b = 5 \times 10^7$ K; $T_e = 5.2 \times 10^5$ K. $1.4 M_\odot$ neutron star with a radius of 16 km, $N_H = 10^{20} \text{cm}^{-2}$. The observer’s distances are adjusted to avoid superposition of the light curves (the shape of the light curves and the value of the pulsed fraction are independent of the distance).

Fig. 8.— Pulsed fraction for the configuration of Fig. 4 and 6 but with different column densities N_H as indicated. The continuous curve shows the pulsed fraction as would be obtained with a perfect detector, thus independent of the column density.

Fig. 9.— Gravitational lensing of the light curves: orthogonal rotator. Sequence of light curves from a $1.4 M_\odot$ neutron star with decreasing radii from ∞ (i.e., no general relativistic effects) down to 6.25 km. Since the surface temperature, for a given field strength and internal temperature, is proportional to $g_{s14}^{1/4}$ (see Fig. 1) we have forced $g_{s14} = 1$ in calculating the surface temperature distribution: all stars have exactly the same $T_s(\theta, \phi)$ and the effects shown are exclusively due to lensing and red-shift. We took $T_b = 5 \times 10^7$ K, $B_p = 10^{12}$ G and $\alpha = \zeta = 90^\circ$. The distances of the stars are chosen such that the total received flux is the same for all stars and $N_H = 10^{20} \text{cm}^{-2}$. Lowering of the intensity for decreasing radii is due to the red-shift which slowly drives the flux out of the PSPC’s range. Notice that for radii between 8.85 km and 7.3 km the peaks are 90° off-phase with respect to the other cases. Phase 0 corresponds to the dipole pointing toward the observer.

Fig. 10.— Gravitational lensing of the pulsed fraction: same model as Fig. 9 with radii from ∞ down to 6.25 km.

Author's Address

Dany Page: Instituto de Astronomía, U.N.A.M.,
Apdo postal 70-264
04510 MEXICO D.F., México
E-mail : PAGE@ASTROSCU.UNAM.MX

Figure 2

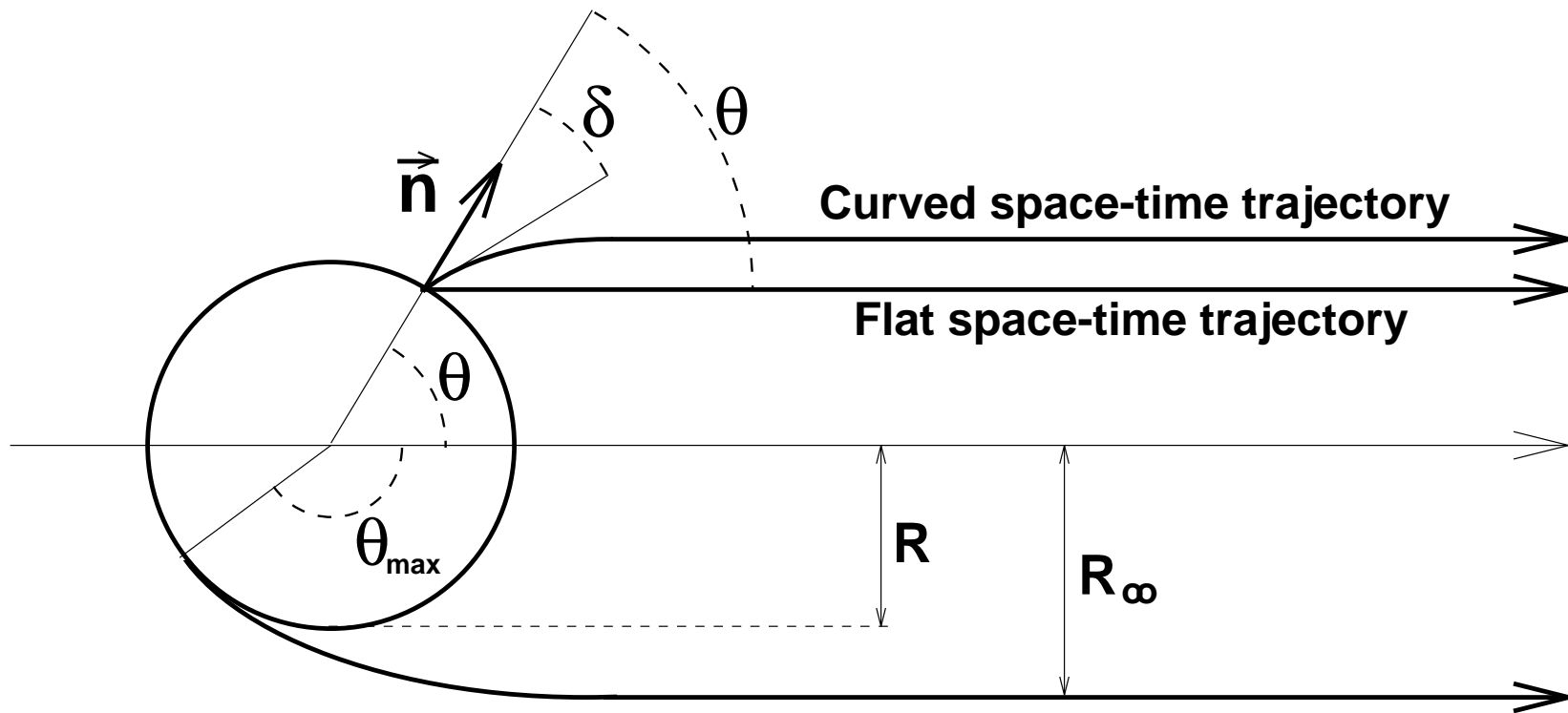


Figure 1

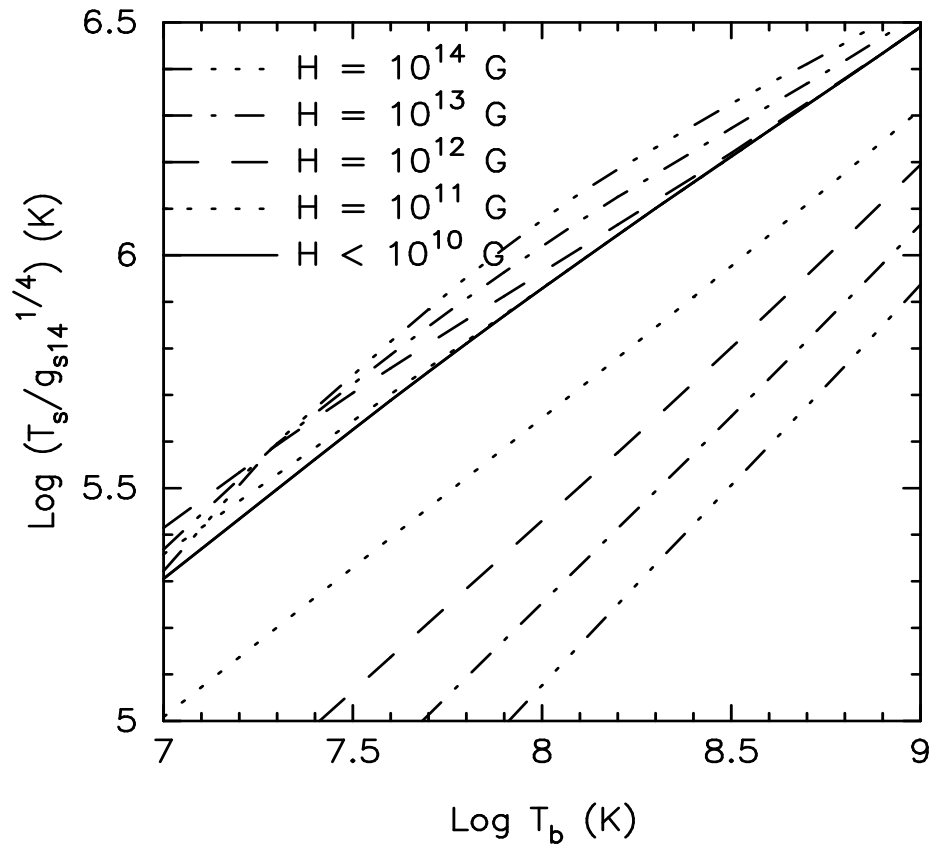


Figure 3

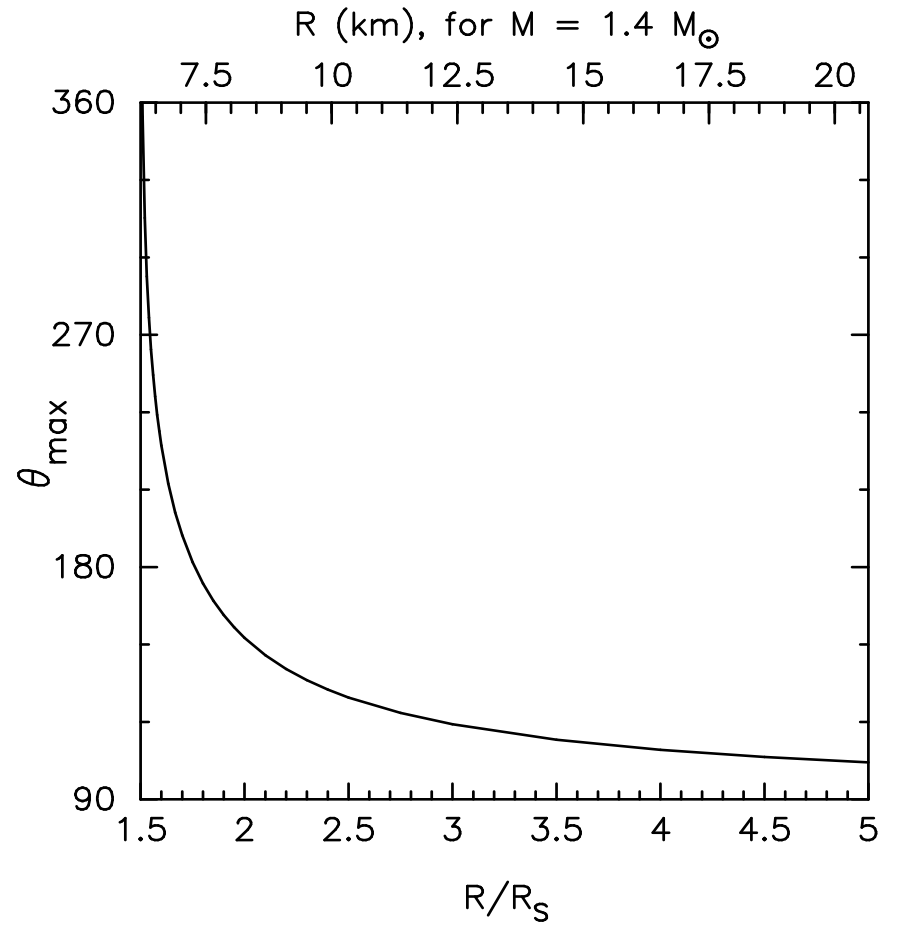


Figure 4

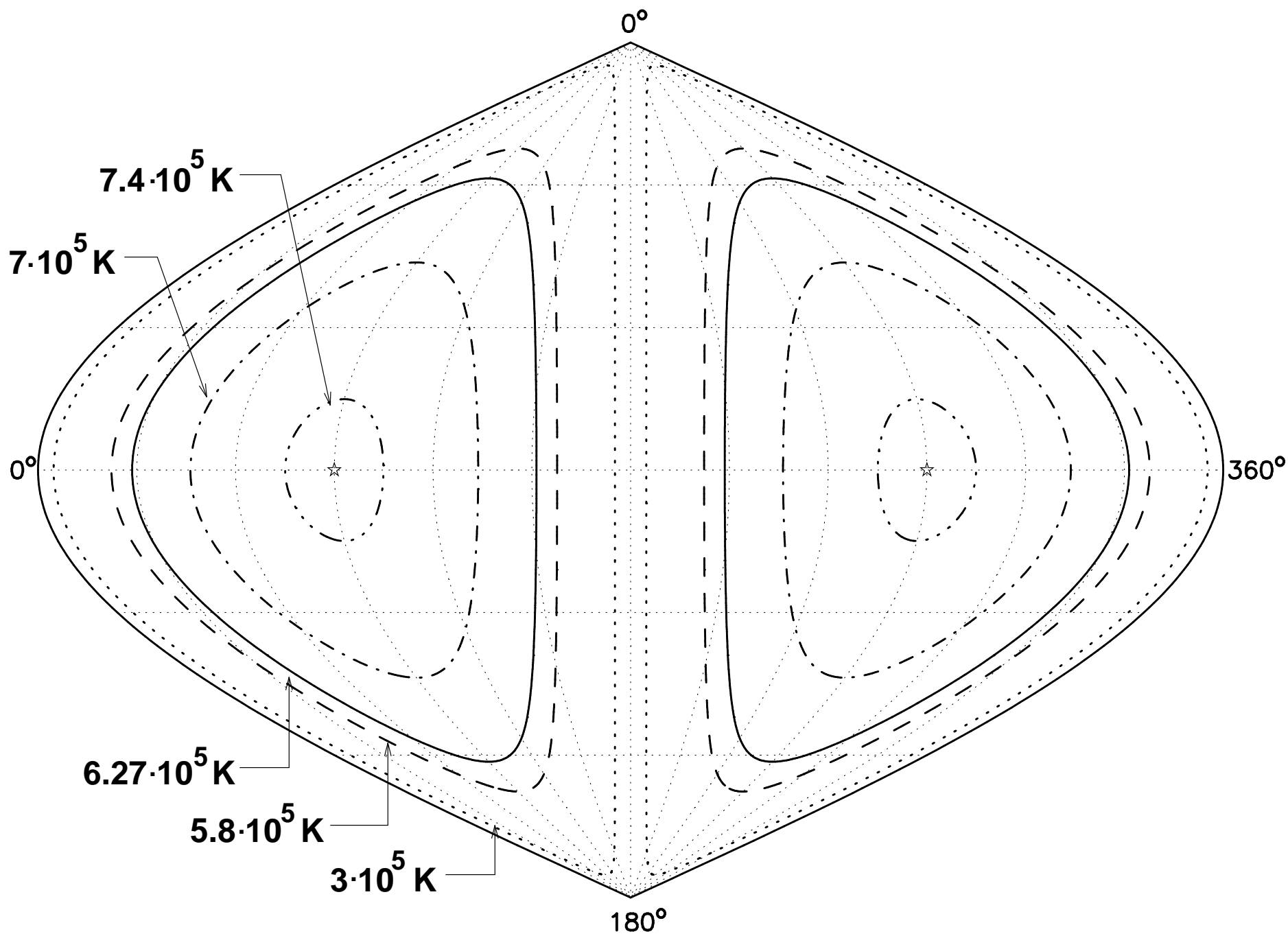


Figure 5a

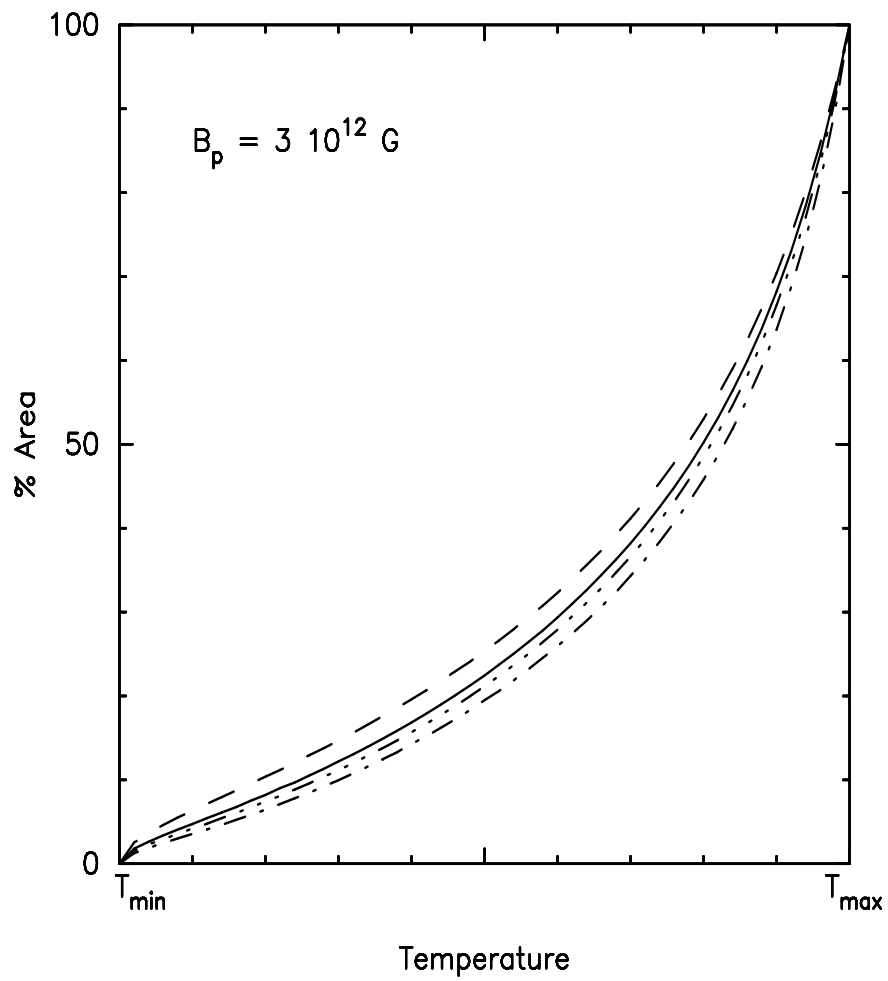


Figure 5b

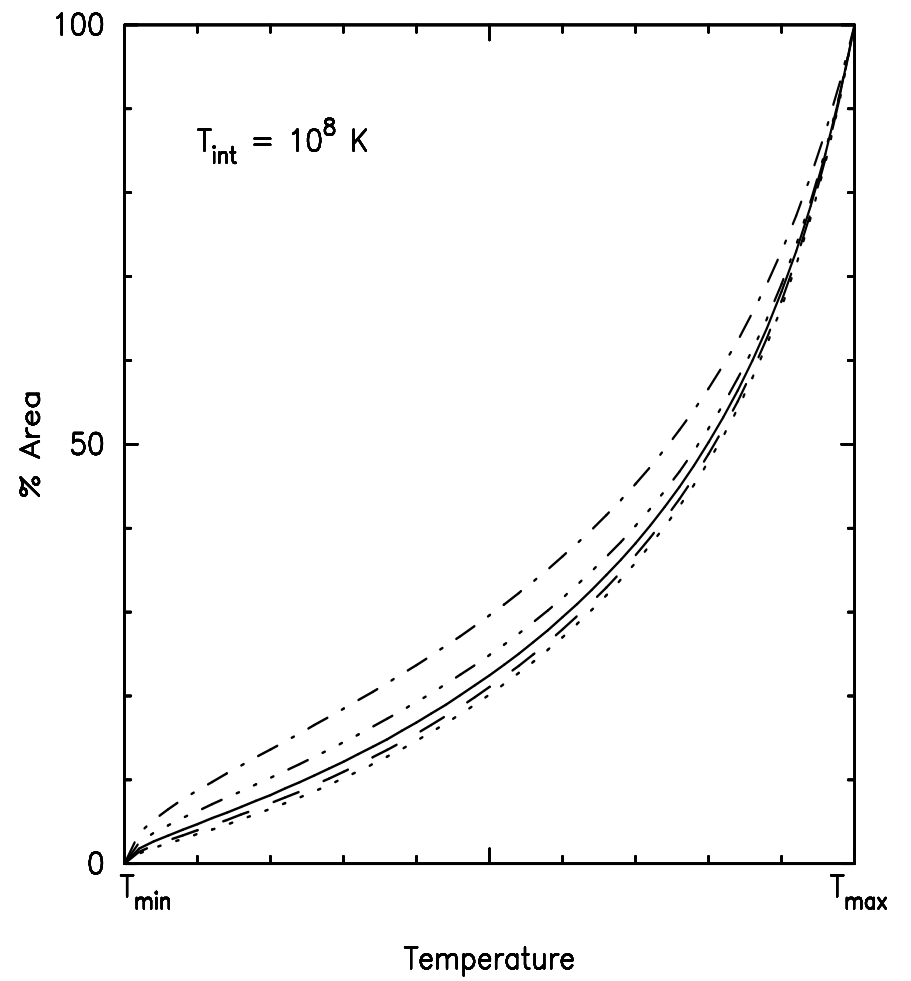


Figure 6

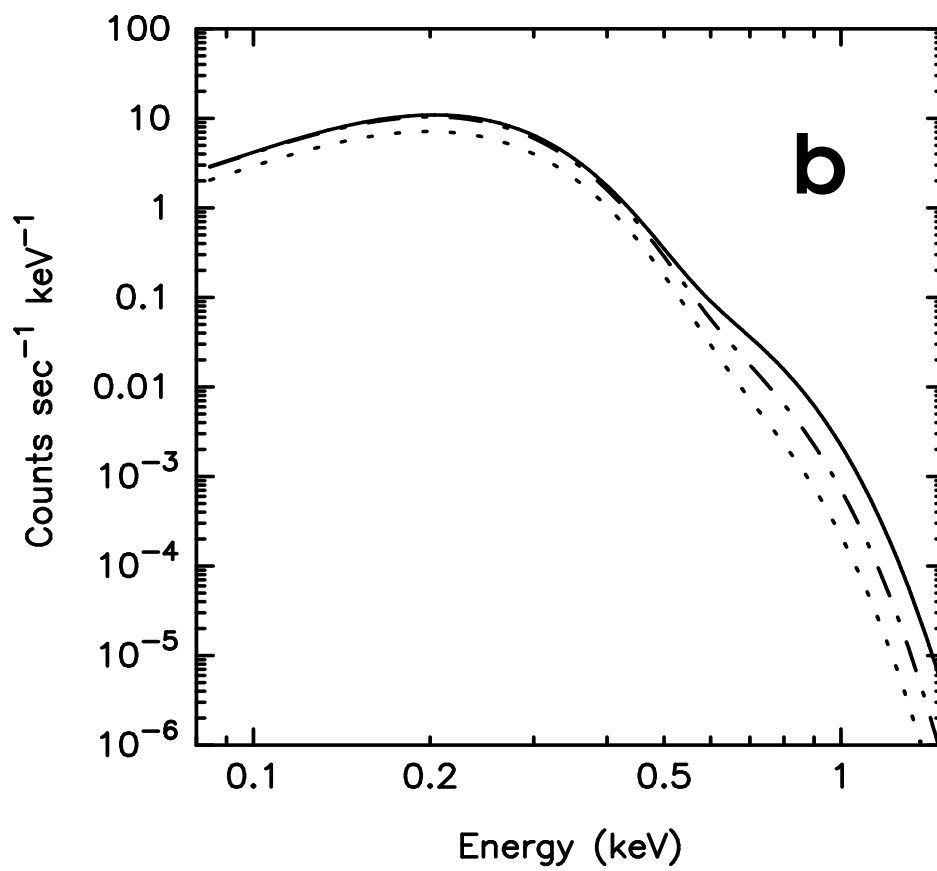
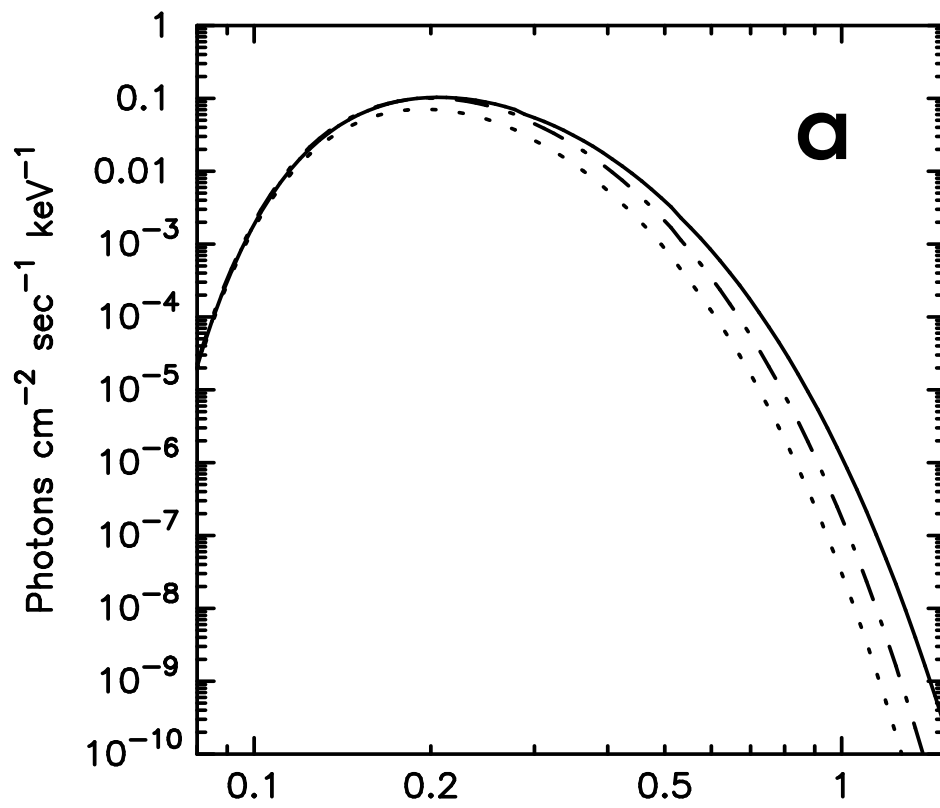


Figure 7a

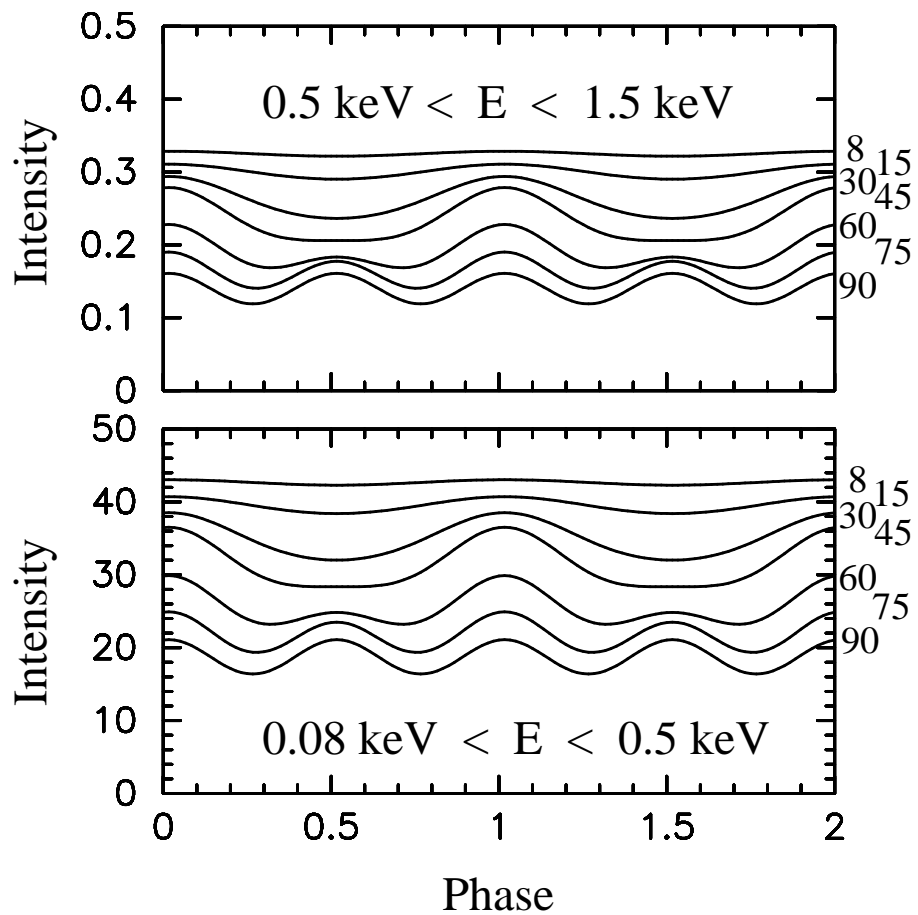


Figure 7b

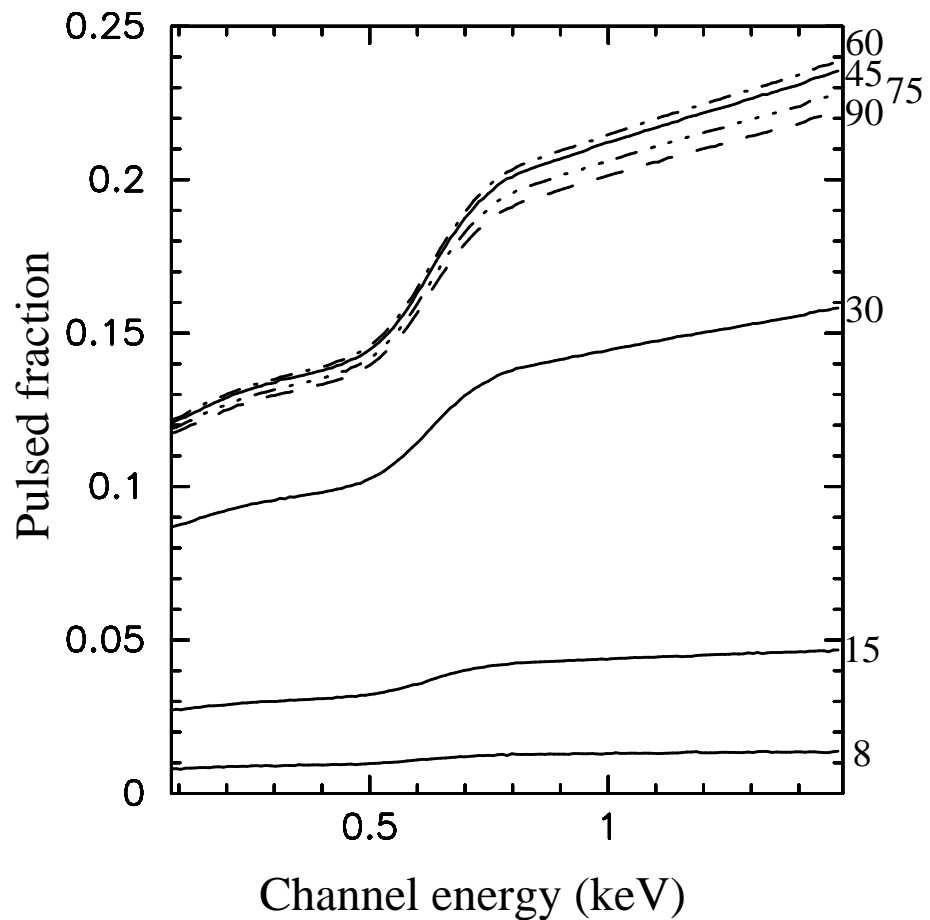


Figure 8

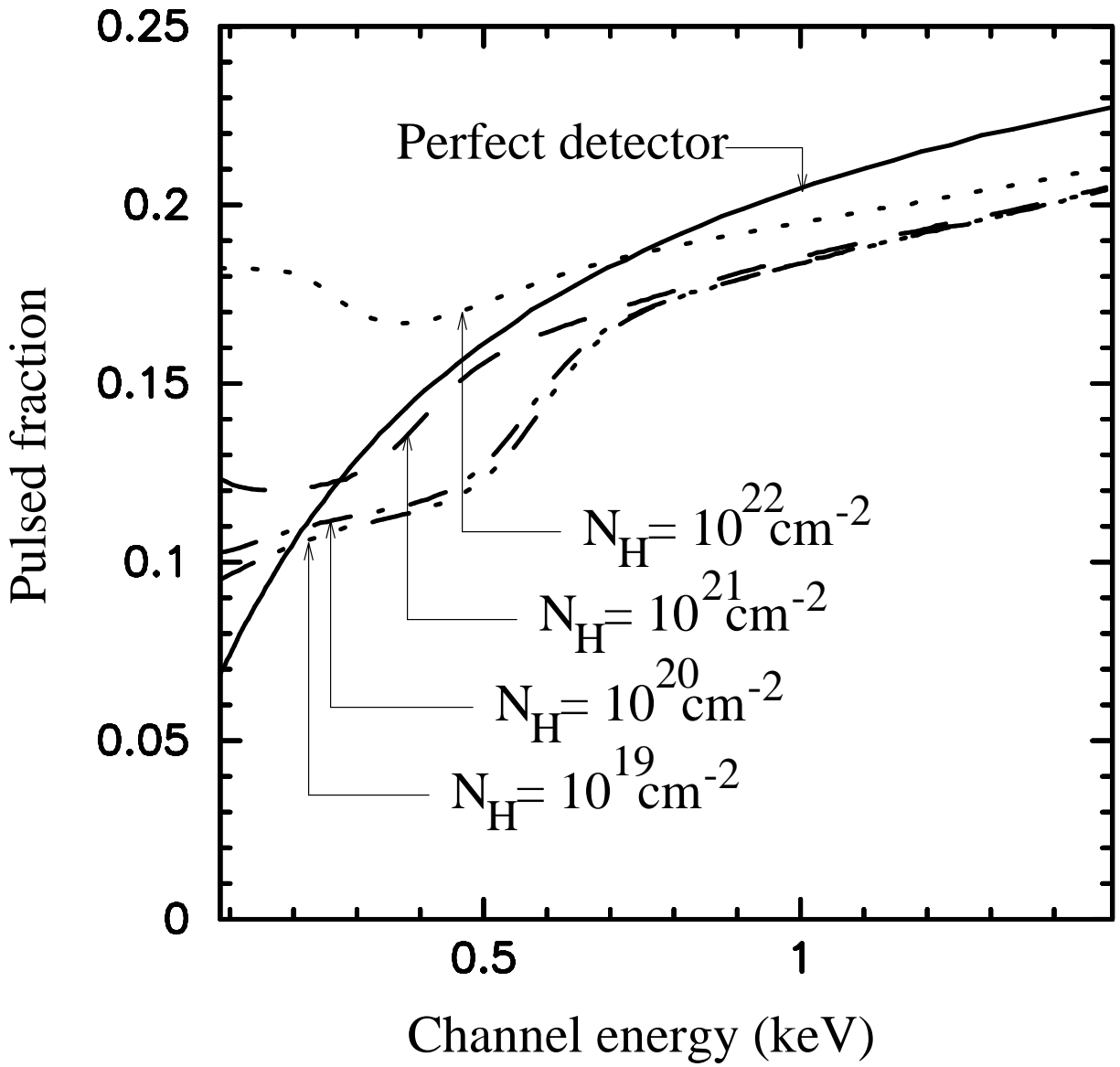


Figure 9

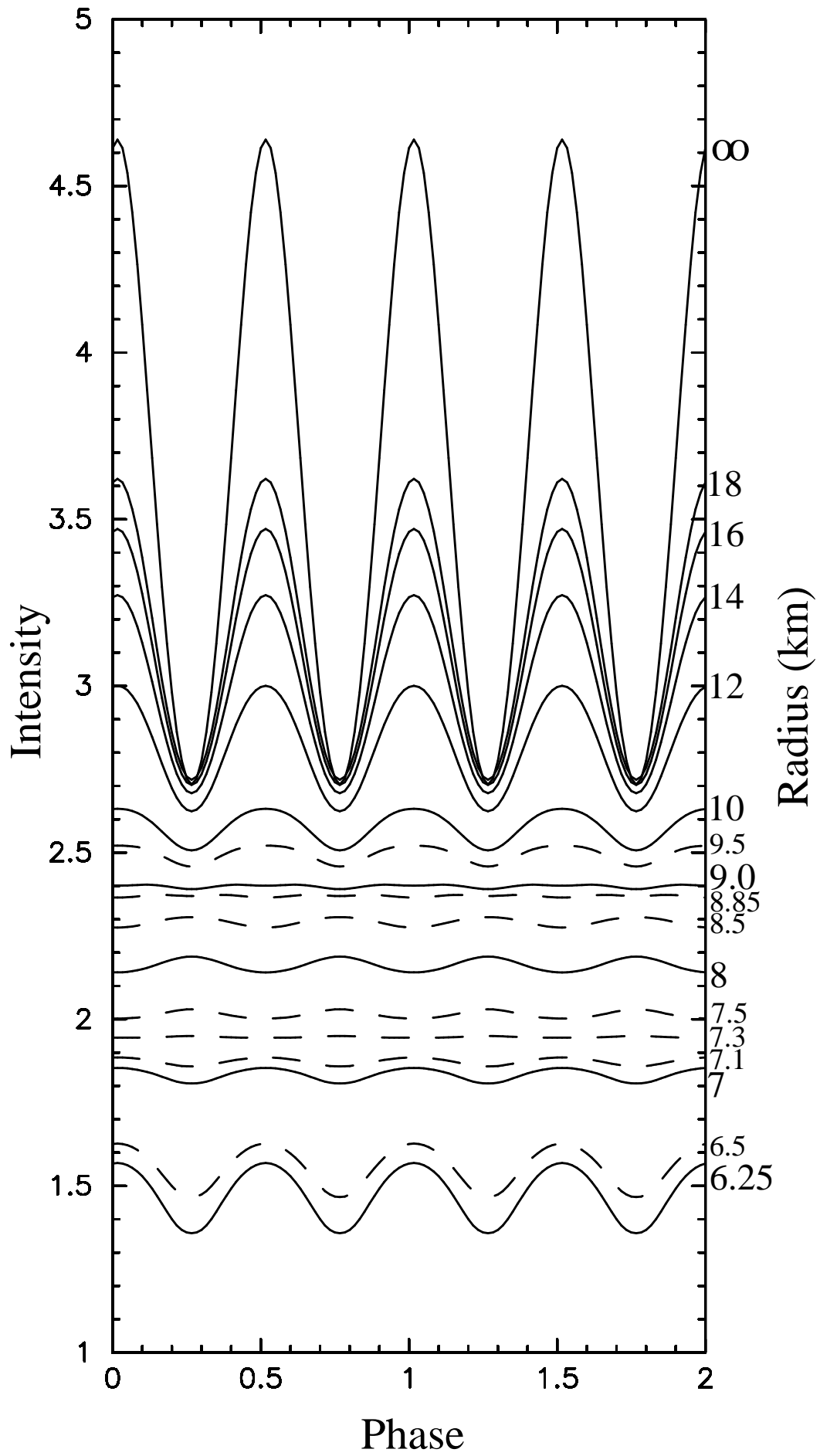


Figure 10

